Earth and Planetary Science Letters 381 (2013) 127–137

Contents lists available at ScienceDirect

Earth and Planetary Science Letters

www.elsevier.com/locate/epsl

Frictional strength and wear-rate of carbonate faults during high-velocity, steady-state sliding

Yuval Boneh [a,1], Amir Sagy [b], Ze'ev Reches [a,*]

[a] School of Geology and Geophysics, University of Oklahoma, Norman, OK 73019, United States
[b] Geological Survey of Israel, 30 Melkhe Israel St., Jerusalem, Israel

ARTICLE INFO

Article history:
Received 16 January 2013
Received in revised form 29 August 2013
Accepted 31 August 2013
Available online xxxx
Editor: P. Shearer

Keywords:
faulting
wear
friction
experimental
high slip velocity

ABSTRACT

We ran an extensive series of shear experiments to test the effect of shear velocity and normal stress on wear-rate and frictional strength. The experiments were conducted on three types of carbonate samples with a rotary shear apparatus on solid, ring-shaped rock samples that slipped for displacements up to tens of meters at slip velocity of $V = 0.002$–0.96 m/s, and normal stress $\sigma_n = 0.25$–6.9 MPa.
The analysis reveals that during steady-state stage, the values of wear-rate and frictional strength depend on both slip velocity and normal stress. The wear-rates at low slip velocity show linear relations to the normal stress (Archard's model), however, at high velocity, $V > 0.5$ m/s, the wear-rates are independent of the normal stress, and may vanish at the highest velocity and normal stress of the present experiments. The steady-state friction coefficient, μ, correlates best with the experimental power-density (= shear stress · slip velocity). We recognized three friction regimes: high $\mu > 0.8$ at low power-density, low $\mu \sim 0.3$ at high power-density, and a transition regime of fast drop of friction coefficient as the power-density increases from 0.03 to 0.3 MW/m^2. Runs of low power-density (high friction) displayed fault surfaces covered with fine-grained gouge, whereas runs of high power-density (low friction) displayed shiny, smooth fault surfaces. We interpret the observed intensity variations of wear-rate and frictional strength as indicating a brittle to ductile transition associated with frictional heating.

1. Introduction

Slipping along faults is associated with friction and wear that depend on multiple, interdependent factors (Fig. 1) such as the intensity of applied loads, fault-zone composition and structure, environmental conditions (fluids chemistry/pressure, humidity and temperature), and slip surface characteristics (e.g., roughness, pore pressure, gouge thickness and grain size). The friction coefficient (Byerlee, 1978), and the wear coefficient (Archard, 1953) are respectively the common parameters for fault strength and wear accumulation rate. Our present objective is to experimentally characterize the connection between frictional strength and wear-rate in carbonate faults, and to test the effects of shear velocity and normal stress on both constitutions.

Wear accumulation volume, G, during shear between two surfaces is assumed (Archard, 1953) to follow the relations of

$$G = K \cdot D \cdot (\sigma_n / H) \quad (1)$$

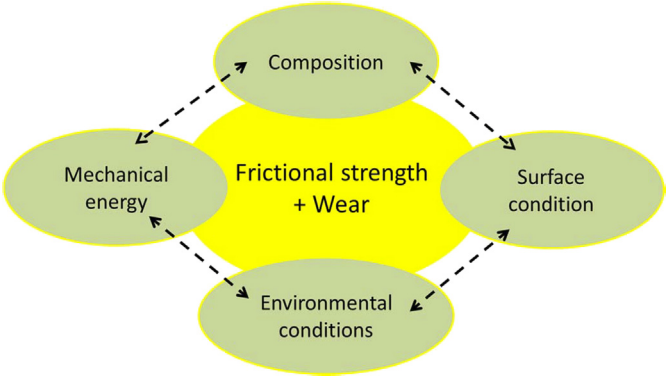

Fig. 1. Conceptual diagram of the controlling factors of wear and friction along faults.

where K (wear coefficient) is related to the material properties and shear conditions, D is the slip distance, σ_n is the normal stress, and H is the hardness of the softer component of the slipping system. This formula is based on the assumption that wear occurs at the real contact area between the sliding surfaces which is restricted to the touching asperities. Queener et al. (1965)

* Corresponding author.
E-mail address: reches@ou.edu (Z. Reches).
[1] Now at: Earth and Planetary Sciences, Washington University, One Brooking Drive, MO, 63130, United States.

0012-821X/$ – see front matter
http://dx.doi.org/10.1016/j.epsl.2013.08.050

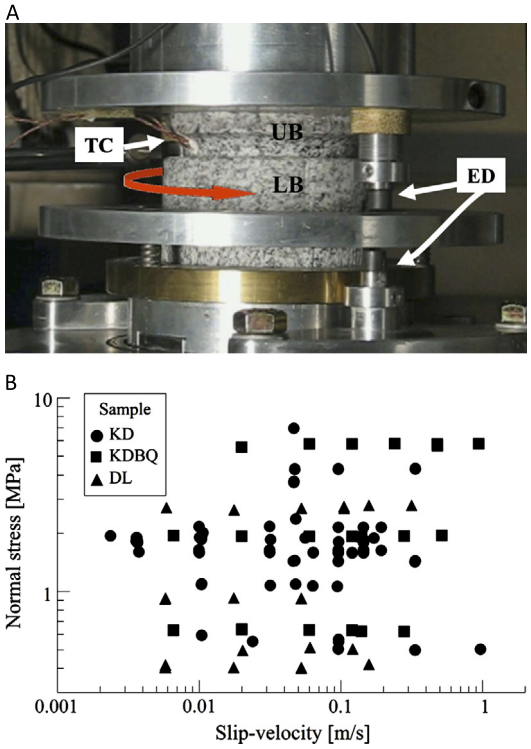

Fig. 2. Experimental setup and mechanical conditions. A. An experimental fault made of Sierra White granite emplaced in the high velocity rotary shear apparatus (Reches and Lockner, 2010). The fault is composed of a lower block (LB) and an upper block (UB), with a ring-shaped contact in the upper block. TC – Thermocouples embedded in the upper block; ED – Eddy current sensors that measure the closure/dilation normal to the fault during slip. B. Range of the experimental normal stress, σ_n, and slip velocity, V, in the present study. KD – runs with Kasota dolomite (circles); KDBQ – run with a fault composed of Kasota dolomite on Blue quartzite (squares); DL – runs with Dover limestone (triangles).

recognized that wear exhibits two distinct stages. An initial, transient stage, which is regarded as 'running-in' of the slip surfaces, exhibits very intense wear-rate due to interaction and failure of the prominent asperities. This stage evolves into steady-state with a modest to low, constant wear-rate. Later tribological analyses indicated that wear of metals depends on the *combined* effect of normal stress and slip velocity (Soda et al., 1975; Lim et al., 1987; Stupak et al., 1990; Kong and Ashby, 1992; Kishore et al., 2000), and not solely on the normal stress.

The above concepts were adopted to experimental studies of faulting and rock wear in which intact rock blocks slipped against each other (Yoshioka, 1986; Biegel et al., 1992; Boitnott et al., 1992; Wang and Scholz, 1994). Wang and Scholz (1994) experiments were conducted at low slip velocity (150 μm/s) and displacements up to 2 m, and showed good agreement with Archard's model. Scholz (1987) discussed the general correlation between the thickness of gouge zones and the total slip distance of the host faults (also Wilson et al., 2005). Power et al. (1988) assumed that the roughness of natural faults is fractal and therefore their wear is always transient. Nevertheless, they also suggested a linear relationship between slip distance and wear volume because larger asperities are statistically more common as slip increases (Power et al., 1988). Recently, Hirose et al. (2012) revealed more complicated relations in experiments of higher velocity (up to 0.27 m/s) and longer displacements (up to 220 m). They found that the wear-rates of granite and diorite samples displayed power and exponential relations to the normal stress, and not the linear relations predicted by Archard (1953).

We investigate here the effects of two controlling factors, slip velocity and normal stress, on the wear and friction of carbonate faults. The analysis is based on experimental measurements on cylindrical samples (Fig. 2A) sheared in a rotary shear apparatus at a wide range of normal stresses and slip velocities (Fig. 2B). A central component of the experiments is the continuous monitoring of fault-normal-displacement, the records of which were used to determine the continuous wear-rate. In addition, we measured shear stress, temperature and slip distance, and used these measurements to discuss the apparent correlation between steady-state wear-rate reduction, slip weakening and temperature increase. The experimental observations are used to examine the validity of wear models and to estimate fault frictional strength at in-situ conditions.

2. Experimental settings

We used a rotary shear apparatus capable of applying normal stresses up to 35 MPa, slip velocities of 0.001 to 2 m/s, and unlimited slip distance (Appendix A, Fig. 11). Continuous monitoring up to 10 kHz recording rate included measurement of normal load, shear load, slip velocity, fault normal displacement, and sample temperature. Details of the experimental systems are outlined in Appendix A.

The experimental faults are made of two cylindrical blocks, the lower one has a flat surface and the upper one has a raised ring structure with dimensions of either 5.40 cm and 7.60 cm as inner and outer diameters, respectively, or 6.32 cm and 8.32 cm as inner and outer diameters, respectively (Figs. 11, 12). We used the mean radius for velocity calculations. Three types of experimental faults were used: (1) a fault made of two Kasota dolomite (KD) blocks; (2) a fault made of two Dover limestone (DL) blocks; and (3) a fault made of one Kasota dolomite upper block and a harder Blue quartzite (KDBQ) lower block. This setup provides a bi-material fault with compositional and hardness contrast. Sample blocks were ground flat, roughened with #600 SiC grit and dried for 24 hr at 100 °C. The experiments were performed at room temperature (~20 °C) and room humidity. The sample temperature during the experiment was measured with one or two thermocouples embedded within the rock at a distance of 3 mm from the sliding surface. Most runs were conducted without opening the two blocks between experiments, whereas in some runs, the experimental fault was opened for gouge collection and inspection. We performed 87 experiments with slip distances of 2 m to 28 m at slip velocity of 0.002 m/s to 0.96 m/s, and normal stresses between 0.25 MPa to 6.9 MPa (Fig. 2B). These experiments include 72 constant-velocity run (DL – 23, KD – 28, KDBQ – 21) and 15 velocity-stepping runs (with 2–6 velocity steps) with Kasota dolomite.

Three methods have been used to calculate wear: (1) Weight of wear products collected from the sliding surfaces (Wang and Scholz, 1994); (2) Wear volume determined from fault-normal-displacement (Reches and Lockner, 2010); and (3) Optical measurements of the worn surfaces. We used the second method since it is the only one that allows continuous measurement of wear without disruption of the experiment or modification of the fault surfaces.

Wear-rate calculations are based on the measurement of the Fault Normal Displacement (FND), which is the displacement normal to the fault surface measured by two or four eddy-currents sensors (Figs. 2A, 12). These non-contact sensors detect displacement by magnetic field changes with an accuracy of ~1 μm. The sensors measure the distance change between the upper and lower blocks. Details of the wear-rate calculations appear in Appendix A.

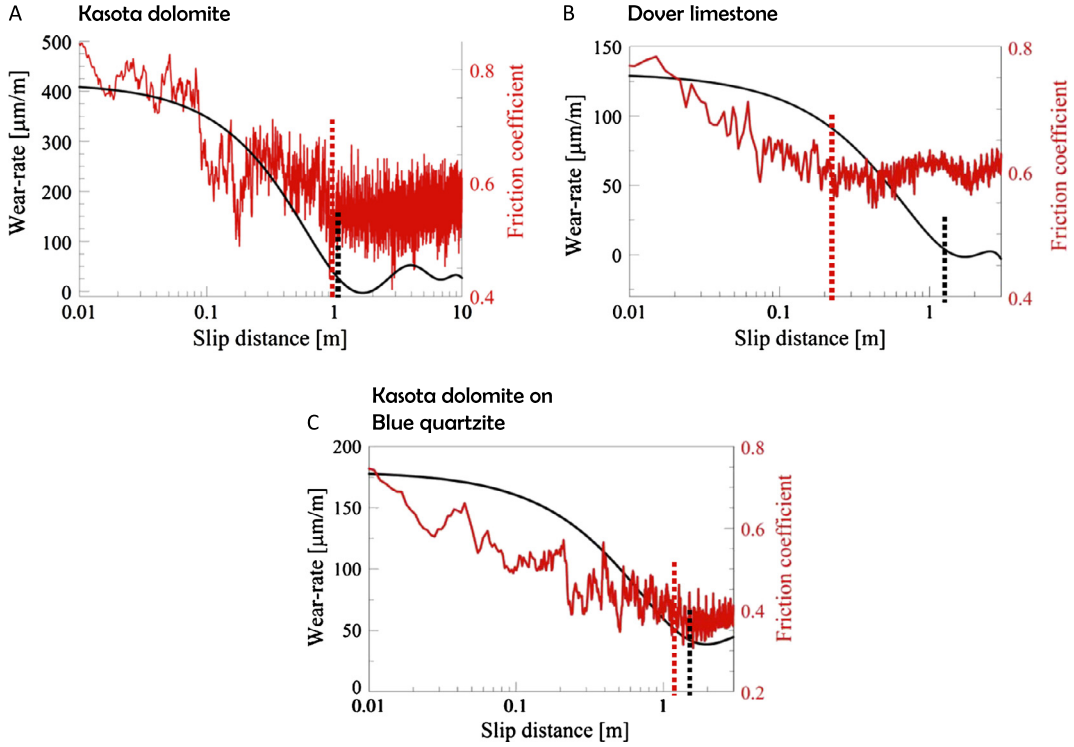

Fig. 3. Typical evolution of wear-rate (black curve) and friction coefficient (red curve) during three shear experiments. A. Kasota dolomite at $\sigma_n = 1.85$ MPa, and $V = 0.14$ m/s. B. Dover limestone at $\sigma_n = 2.7$ MPa, and $V = 0.11$ m/s. C. Kasota dolomite on Blue quartzite at $\sigma_n = 5.7$ MPa, and $V = 0.12$ m/s. Note an initial, transient stage (running-in) of high values of wear-rate and friction coefficients that decrease gradually to lower, quasi-constant, steady-state values, with corresponding critical distances for the transition (dotted, vertical lines of corresponding colors). (For interpretation of the references to color in this figure, the reader is referred to the web version of this article.)

3. Experimental observations

3.1. Evolution of wear, wear-rate and strength

In our experiments, the wear-rate and the frictional strength evolved with time and slip distance, similarly to previous observations (Queener et al., 1965; Power et al., 1988; Wang and Scholz, 1994). The early stage of the slip displayed high values of wear-rates and friction coefficients (Fig. 3) that correspond to the transient, running-in stage. Significantly lower values of both wear-rate and friction coefficient evolved into the steady-state stage (Figs. 3A–C). Boneh et al. (submitted for publication) found that the wear-rate (black curves) and the friction coefficient (red curves) evolve in similar style and over similar distances (1–3 m) during the running-in stage (Fig. 3). They discuss this transition in details, and here we focus on the wear-rates at steady-state.

3.2. Steady-state wear-rate

One of our most significant observations is demonstrated in Fig. 4 that displays the steady-state wear-rates for four sets of experiments in Dover limestone (DL) (Fig. 4A) and four sets in Kasota dolomite–Blue quartzite sample (KDBQ) (Fig. 4B). Each experiment was run at a constant velocity that ranged from 0.006 to 0.3 m/s, and at different normal stresses. In Figs. 4A and 4B, the wear-rates of low velocity runs are marked by a blue, dashed ellipse, and the high velocity runs are marked by a red, dashed ellipse. Two features are apparent in these graphs. First, at slip velocity $\leqslant$0.1 m/s the wear-rates increase quasi-linearly with the experimental normal stresses (green and blue dashed lines in Fig. 4), in agreement with Archard's model. Second, the wear-rates are lower at higher slip velocities, and this is particularly clear at the highest normal stresses in both samples. These observations suggest that steady-state wear-rates depend on both slip velocity and normal stress. Fig. 4A further demonstrates that the wear-rates practically vanish at the highest normal stresses for Dover limestone.

Thus, the observations indicate that in carbonate rocks the steady-state wear-rates (1) depend on both slip velocity and normal stress, and (2) approach zero at high stresses and high slip velocities. These results deviate from Archard's model that predicts linear increase of wear-rates with increasing normal stress. This model was based on wear of real area contacting asperities, and thus, our observations suggest a different wear mechanism as discussed later.

3.3. Steady-state friction coefficient

The results of the experiments also indicate that the measured friction coefficients of the carbonate samples depend on both slip velocity and normal stress. The experimental friction coefficients, μ, are displayed in Fig. 5A as a function of normal stress, and are divided into three velocity groups ($V < 0.1$ m/s, $V = 0.1$–0.3 m/s, and $V > 0.3$ m/s). For these three velocity groups, the friction coefficients decrease with increasing normal stress. The same friction data are plotted in Fig. 5B as a function of the power-density, PD – the rate of mechanical energy dissipated during the experiments,

$$\mathrm{PD} = \tau \cdot V \tag{2}$$

where τ is the shear stress and V is the slip velocity; in our experiments, the PD range was 0.002–1.0 MW/m^2. PD is an effective parameter to characterize the mechanical loading during high-velocity shear experiments (Di Toro et al., 2011; Brown and Fialko, 2012; Chang et al., 2012).

Fig. 5B displays the steady-state friction coefficients of our three carbonate rocks with the coefficients of marble samples (Han et al., 2007). The plot shows similar distribution of the DL and KDBQ data, and somewhat different distribution for the KD results. The marble data fit the general trend of our samples, but reached lower

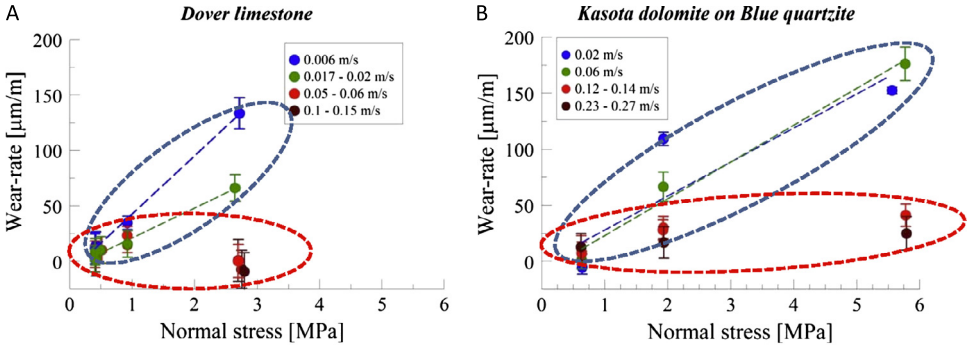

Fig. 4. Steady-state wear-rates as function of the applied normal stresses and slip velocity (inset) for Dover limestone runs (A), and Kasota dolomite on Blue quartzite runs (B). The wear-rates data were grouped according to the slip velocity, and each velocity group with at least three data points was plotted. Note: The wear-rates increase with normal stresses under low slip velocity experiments (encircled by blue, dotted line), whereas the wear-rates drop drastically (almost vanishing) under high slip velocities (encircled by red, dotted line).

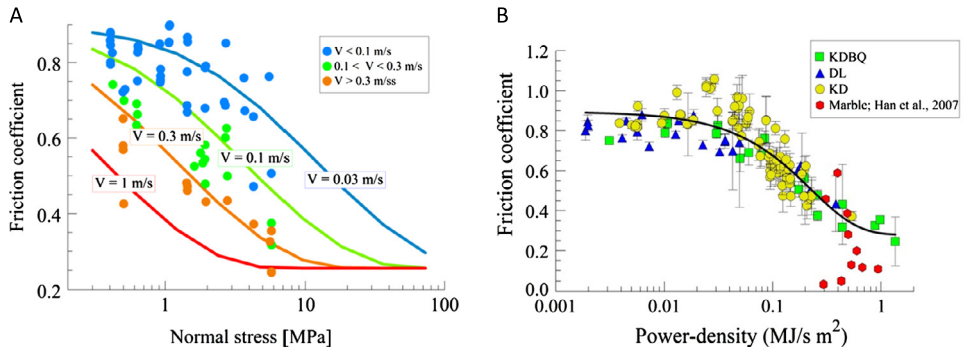

Fig. 5. A. Steady-state, experimental friction coefficients as function of normal stress for all experiments. The friction coefficients are grouped in three classes of slip velocity (inset), and the expected friction coefficient distribution, which was calculated from the best-fit curve in B (text), are plotted by colored curves. B. Steady-state, experimental friction coefficients (with error bars) as function of power-density (PD = shear stress times slip velocity) (see text). The best fit in B (black curve) is $\mu = 0.28 + 0.61 \cdot 0.012^{PD}$. The data of Han et al. (2007) for shearing marble are plotted as red circle.

friction coefficient at high power-density. We searched here for a general, common trend of the three types of carbonate samples, and fit all our data with a best fit curve regardless of the small trend differences. This fit curve (black) is

$$\mu = 0.28 + 0.61 \cdot 0.012^{PD}. \quad (3)$$

The friction–PD curve in Fig. 5B reveals three regimes of frictional strength. First, at low power-density of PD < 0.03, the friction coefficients are high, $\mu > 0.8$, and relatively constant for DL and KDBQ, and slightly rising for KD. Second, at PD > 0.3, the friction coefficients are low for all lithology types, with a lower bound of $\mu \cong 0.28$ for PD > 1. Even lower friction coefficients of $\mu \cong 0.1$ were found in this regime (Han et al., 2007, 2010; Oohashi et al., 2011). The third regime of PD = 0.03–0.3 is a transition between the other two; the controlling mechanism for these regimes is discussed later.

We use Eqs. (2) and (3) to calculate the predicted friction coefficients for four values of slip velocity (0.03, 0.1, 0.3 and 1 m/s) at normal stresses up to 100 MPa. The calculated values are plotted as colored curves in Fig. 5A, and as expected show good fit to the observed friction coefficients (colored dots). These results indicate that the friction coefficient is related to the *combination* of slip velocity and normal stress. This relation (Eq. (3), Fig. 5A) reflects the fault lithology (carbonates) and the experimental conditions (unconfined rock sample at room temperature and humidity). Fig. 5A indicates that at similar slip conditions, the frictional strength of a carbonate fault is low, $\mu = 0.28$–0.35, even at low velocity of $V = 0.03$ m/s, if the normal stress is relatively high, for example at $\sigma_n > 50$ MPa.

3.4. Steady-state failure envelopes

The failure envelopes of the three rock types (Figs. 6A–C) suggest increasing of ductility in the carbonate faults slipping at high velocity. In these plots, the failure envelopes are grouped according to the experimental velocity, and the envelopes were calculated as best-fit power of the form $\tau = a \cdot \sigma_n^b$ (curve parameters in figure caption). The b values vary systematically with slip velocity: $b \sim 1$ (linear Coulomb envelope) at low velocity and $b \sim 0.65$ at the highest experimental velocity (Fig. 6D). In non-linear failure envelopes with $b < 1$, decreasing of the friction coefficient is reflected by the decreasing of the local slope with increasing normal stress. This decreasing of frictional resistance is a distinct property of carbonate ductility that can arise either by raising temperature (Heard, 1960) or by raising confining pressure (Handin and Hager, 1957; Handin et al., 1967; Byerlee, 1968). In the present experiments, the b values and the corresponding frictional strength decrease with increasing slip velocity (Fig. 6D), and because the normal stresses in the present experiments are constants and significantly lower than those of Heard (1960) and Handin et al. (1967), we deduce that the ductility increases is due to frictional heating at the higher velocities. Thus, we conclude, and further discuss later, that the slip along carbonate faults at high velocity activates fault-zone ductility.

3.5. Fault surface characterizations

Experimental carbonate faults that were sheared at high power-density (PD) displayed partial to almost complete coverage by

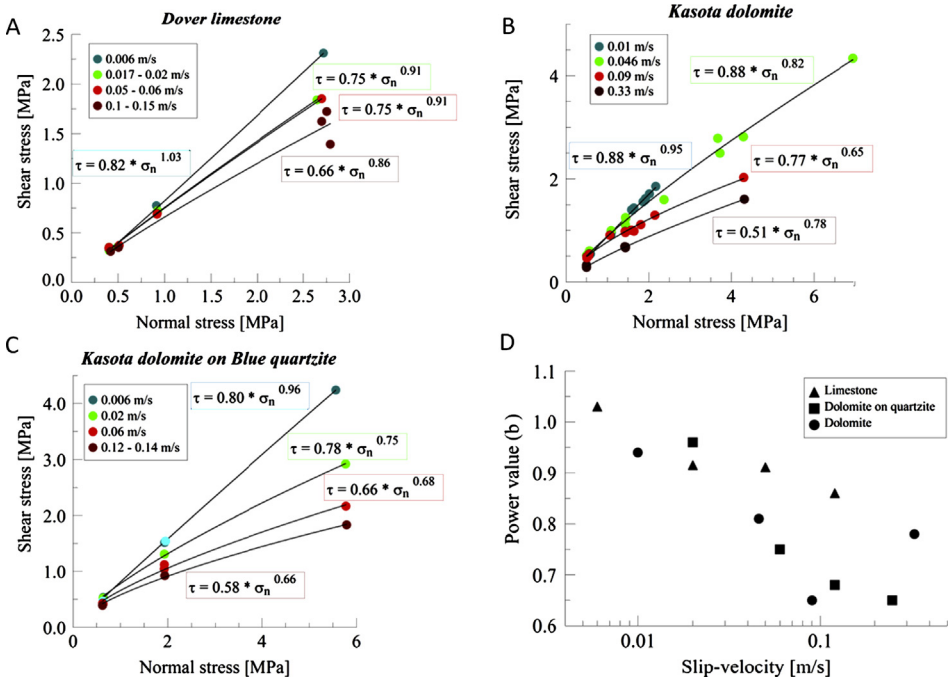

Fig. 6. Mohr diagrams with shear failure envelopes in present experiments. A–C. Steady-state shear stress against normal stress; dot colors indicate the slip velocities (inset); best-fit, power-law curves of the shape $y = ax^b$ were calculated and marked for DL (A), KD (B) and KDBQ (C). D. The power values, b, from A–C are plotted as function of slip velocity. Note that b is about unity (= linear, Coulomb envelope) at low slip velocities, and decreasing b with increasing slip velocity that indicates lower friction coefficients (text).

polished, shinning surfaces (Figs. 7C, D). These high PD runs also showed low wear-rates and low friction coefficients that were discussed above (Figs. 4, 5). We examined these shinning surfaces under ×50 magnification (binocular), and discuss here the main observations. Detailed multi-scale geometrical analysis of similar samples with down to 10 nm resolution was presented by Chen et al. (2013).

Experimental faults that were sheared at low PD ($<$0.03 MW/m^2) typically displayed surfaces covered with a thin gouge layer that was formed during shear (Fig. 7A). In an unconfined experiment, the excessive gouge material was ejected out of the slipping ring and accumulated in heaps inside and outside the ring (Figs. 7A, 12). At intermediate power-density, small islands of cohesive shiny surfaces surrounded by gouge powder started to appear (Fig. 7B); the number and cumulative area of these patches increases with increasing PD (Figs. 7B, C). The shiny, polished slip surfaces are darker and glassier in appearance than the original sample surface (Fig. 7C), and their light reflectance indicates high smoothness with mean roughness $<$1 μm. The shiny surfaces also acquire anisotropic roughness: they are highly smooth parallel to slip direction, and wavy normal to it as was measured with Atomic-Force-Microscope (Chen et al., 2013). This anisotropy corresponds to the roughness anisotropy observed along natural faults (Sagy and Brodsky, 2009; Resor and Meer, 2009). The small patches of shiny surfaces that appear at intermediate velocity, $V = 0.05$ m/s (Fig. 7B) most likely developed at areas with locally elevated shear stresses at asperities that led to a local increase of frictional heating (Brown and Fialko, 2012). At higher velocity, $V = 0.36$ m/s, with higher frictional heating, most of the fault surface becomes shinny (Fig. 7C, D). Similar observations of local temperature increase at relatively low slip velocities were documented by Brown and Fialko (2012). Field occurrence of shiny surfaces that cover the entire face of active carbonate faults has recently been interpreted as indicating fault slip at seismic velocity due to associated frictional heating (Siman-Tov et al., 2013).

4. Discussion

4.1. Maps of carbonate wear-rates and friction coefficients

Our above observations (Figs. 4–7) demonstrate the dependence of wear-rate and friction coefficient on slip velocity and normal stress. This dependency can also be presented by wear and friction maps (Fig. 8), that are commonly used for characterization of wear resistance of industrials materials in the field of normal stress and slip velocity (Vingsbo and Soderberg, 1988; Hutchings, 1992; Lim, 2002). These maps synthesize experimental data to evaluate wear intensity and wear mechanisms for a given material composition (Wang et al., 1995; Lim, 1998).

We present here a wear-map and a friction-map (Fig. 8) for displaying the combined effect of velocity and stress on carbonate faults. Results of runs with short slip distance ($D < 2$ m) were excluded from the wear-map as they may include the running-in regime.

The wear-map (Fig. 8A) shows two regimes of wear intensity separated by a dotted contour line: *mild wear-rate* in the low normal stress regime and the high velocity regime, and *intense wear-rate* in the regime of high normal stress and low velocity. The friction-map (Fig. 8B) shows a systematic decrease in friction coefficient at higher velocities and higher normal stresses. The friction coefficient values are separated by contours of equal PD with values of 0.1 and 0.3 MW/m^2. These wear and friction maps (Fig. 8) are useful tools for characterizing wear-rate and friction at a wide range of conditions, including extrapolation to natural conditions by additional experiments in the relevant velocity and normal stress.

In the present case of carbonate rocks, the maps coordinates are slip velocity and normal stress, but one can use other relevant coordinates such as temperature, fault roughness or composition. Furthermore, as wear-rate depends on many parameters (Fig. 1), the complete wear-rate map (and friction map) should be of n dimensions. While the construction of such n-dimensional space

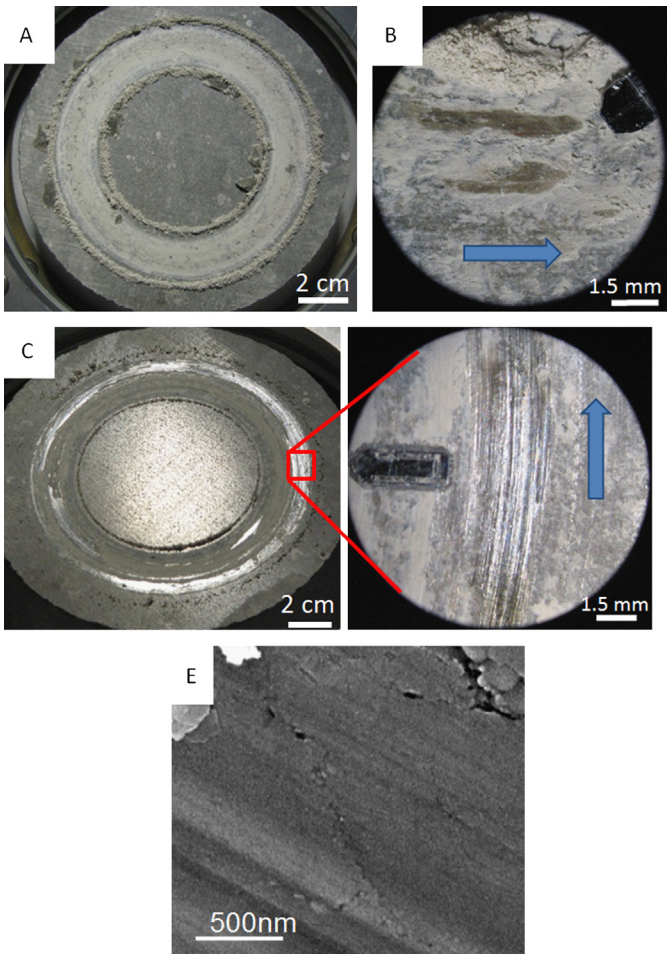

Fig. 7. Slip surfaces of the lower, rotating block of Dover limestone experiments; these photos are 'as is' views of the open fault after the run. A. General view of the lower block run at $V = 0.003$ m/s to a distance of 3 m, at $\sigma_n = 1.3$ MPa, and with steady-state $\mu = 0.80$. The bright ring of fine-grain gouge powder matched the ring-shaped contact surface of the upper block. The circular heaps inside and outside the gouge-covered ring are ejected gouge powder. B. Experimental fault from run at $V = 0.05$ m/s to a distance of 3.5 m, under $\sigma_n = 0.90$ MPa, and with steady-state $\mu = 0.75$ that displays two small, elongated patches of shiny, dark, smooth surface surrounded by bright gouge (note scale); arrow indicate slip direction. C. General view of the lower block of run at $V = 0.36$ m/s to a distance of 3.7 m, at $\sigma_n = 1.4$ MPa, and with steady-state $\mu = 0.50$. At this higher slip velocity, large portion (~25%) of the ring area is covered by shiny, dark surface (text). D. Detail of C with close-up of the shiny surface. E. Scanning-electron-microscope view of the shiny, striated surface of high velocity KD fault; note well compacted grains of tens nm in size.

may be difficult, limiting the dependence to one variable, e.g., normal stress in Archard's model, is clearly insufficient.

4.2. A geo-tribological view of steady-state wear

Fault sliding may occur in two tribological styles: a 'two-body' mode in which bare rock blocks are in direct contact along their asperities (Fig. 9A), or a 'three-body' mode in which the two blocks are separated by a liquid or a solid lubricant (Fig. 9B) (Rabinowicz et al., 1961; Godet, 1984; Ludema, 1996). Boneh et al. (submitted for publication) found that the shear along experimental faults evolved from two-body mode to three-body mode when the fault surfaces were gradually covered with gouge powder as slip distance increased (running-in stage). After slip distance of 0.5–3.0 m, the rock blocks were separated by a 50–200 μm thick gouge layer (Fig. 7A) (Reches and Lockner, 2010). Once the fault zone is at this three-body mode, the asperities are no longer in direct contact (Fig. 9B), the shear is accommodated within the gouge layer, and the asperity-related wear drastically reduces or even diminishes. We envision that a different mechanism dominates the wear at this configuration. A clue to this mechanism may be deduced from Fig. 9C that displays wear-rates as function of the friction coefficients for experiments run at high normal stress of $\sigma_n > 2$ MPa. The data points are scattered, yet the trends for the three fault types are similar and indicate that the wear-rates are proportional to the measured friction coefficients for the experimental faults. These observations led us (Lyakhovsky et al., submitted for publication) to develop a model for steady-state wear. The model assumes that at three-body configuration the wear occurs at the rock-gouge contact, and that the solid host rock wears by microfracturing induced damage. Lyakhovsky et al. showed that this damage is controlled by the shear stresses at the rock-gouge contact, and suggested that once the microfractures reach a critical density, the solid rock disintegrates and its fragments merge the gouge zone. The model predictions successfully fit the results of the present experiments.

The shear properties of the gouge third-body may be analyzed in terms of global flow that depends on its composition and shear conditions (Fig. 1). A brittle third-body that is composed of large and fine particles (e.g., fault gouge of quartz-bearing rocks) is sheared by granular or powder flow (Sammis and Ben-Zion, 2008; Reches and Lockner, 2010). On the other hand, the gouge may flow as a ductile third-body according to its rheology at the given temperature and grain size (Hutchings, 1992; Descartes and Berthier, 2002). For example, Smith et al. (2013) recently sheared calcite powder at high power-density, and they showed that the shear is localized within a thin layer (tens of μm) of plastically deformed, recrystallized calcite grains. These transitions into more ductile regime strongly depend on the response of fault composition to the loading and shear conditions as anticipated in our opening statement.

4.3. Fault weakening by increasing ductility

The transition from two-body configuration to three-body configuration (Fig. 9) at high-velocity/high normal stress experiments is clearly associated with wear-rates drop to vanishing values (Figs. 3, 8A). As already discussed, this wear-rates drop, which contradicts Archard (1953) model, indicates a reduction asperity contact and asperity failure while the fault shear is accommodated, partly or fully, by flow within the gouge, and Archard's "wear coefficient" (Eq. (1)) depends on slip velocity and may be on normal stress.

Wear and friction reduction in three-body configuration can be explained by a few mechanisms, such as powder lubrication or flash heating. However, the observed variations in wear-rate and friction resistance in the present carbonate faults are better understood by ductility increasing of fault zone. First, the failure envelopes of our experiments are non-linear (Figs. 6A–C), and the non-linearity increases with increasing slip velocity (Fig. 6D). As mentioned above, this non-linearity indicates ductility associated with increasing temperature (Barber et al., 1994). Second, the surfaces of experimental faults that slipped at high velocity (and consequentially elevated temperature) displayed patches of shiny crust which covered part or most of the sliding area. These patches are made of densely packed grains, 10–50 nm in size (Fig. 8E), that form a cohesive, highly smooth surface (Green et al., submitted for publication; Chen et al., 2013), which were most likely formed as bands of ductile flow of heated, ultra-fine gouge grains.

Ductile flow of carbonate rocks strongly depends on temperature and stresses (Heard, 1960; Handin and Hager, 1957). The applied normal stress in the present experiments are relatively low; therefore, the ductility increase is primarily controlled by the frictional heating, which is now evaluated. In the experiments, the

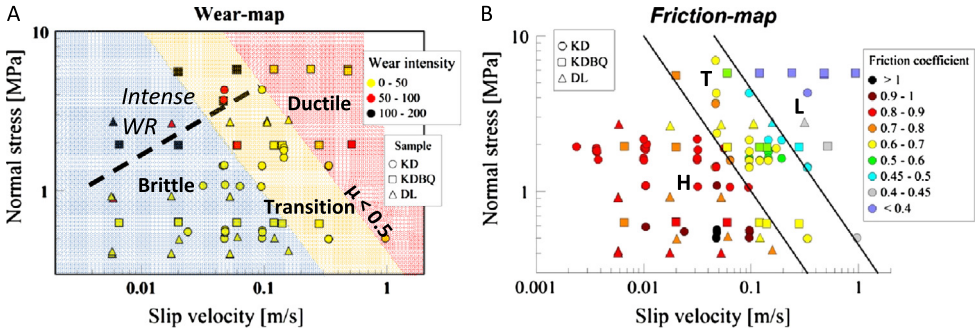

Fig. 8. A. Wear-map of steady-state values as function of normal stress and slip velocity; results of stepping experiments were excluded from this plot. Wear-rate intensities are shown by color and samples lithology by symbols (insets). The dashed line separates between fields of intense and mild wear-rates. B. Friction-map that displays the steady-state values in all present experiments. The friction values are shown by color and samples lithology by symbol (insets). The contours delimit regimes of high (H, $\mu >$ 0.7), low (L, $\mu < 0.5$) and transitional (T) friction coefficients. Following Fig. 5B, these contours are of constant power-density with values of (normal stress·slip velocity) = 0.1 and 0.3 (MW/m^2); these contours bound the interpreted brittle and ductile regimes marked in the wear-map (A) (text).

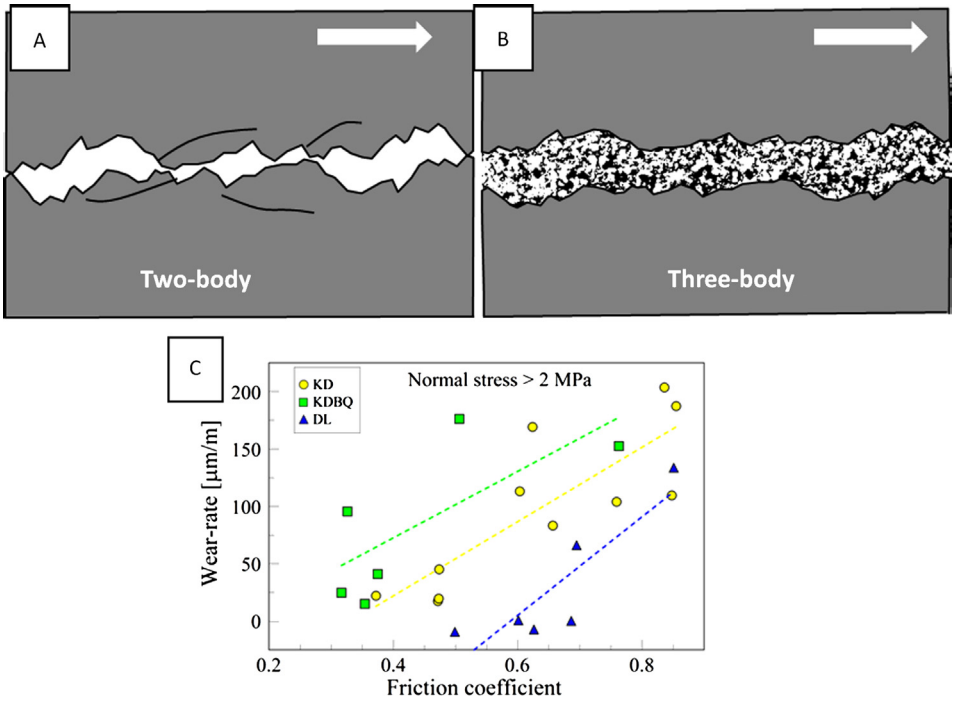

Fig. 9. Schematic illustration of fault zone two-body (A) and three-body modes (B). In two-body mode, the sliding blocks interact at touching asperities/surface roughness, whereas in three-body mode, the sliding blocks are separated by a gouge layer. C. Relations between steady-state wear-rate and frictional strength in all experiments with $\sigma_n > 2$ MPa. Note that for any given frictional strength, the wear-rates are higher for the fault with the harder components: wear-rates of dolomite–quartzite > wear-rates of dolomite > wear-rates of limestone. (For interpretation of the references to color in this figure, the reader is referred to the web version of this article.)

applied mechanical power, PD, is dissipated by frictional heating of the fault surfaces, sample cooling to the surrounding air, gouge formation, and heat diffusion into the rock sample. At steady-state shear of a given experiment, these variables maintain a quasi-constant values, as shown by constant experimental PD, and constant slopes of thermocouple temperature and wear-rate in Dover limestone experiment 2284 (Fig. 10A). Thus, if air cooling also occurs at a constant rate during the steady-state slip, the heating rate of at the thermocouple, T', is a plausible proxy of the rate of frictional heating on the fault surface. We use

$$T' = \frac{\Delta T}{\Delta X}$$

where ΔT and ΔX are the thermocouple temperature rise and the measured slip distance during the entire steady-state stage, respectively; T' units are °C/m. We examine below the relations between this rate and the friction coefficients.

Fig. 10B displays the friction coefficients, μ, and rate of temperature-rise, T', of the three rock types as function of PD. As expected, T' is proportional to the power-density, PD,

$$T' = 76.7 \cdot \mathrm{PD}^{0.47} \quad (r^2 = 0.73) \tag{4}$$

(red, dashed curve in Fig. 9). We already found that the friction coefficients are related to the power-density by Eq. (3) (Fig. 5B),

$$\mu = 0.28 + 0.61 \cdot 0.012^{\mathrm{PD}}$$

(blue, dashed curve in Fig. 10B). The clear inverse dependence of μ and T' on PD reveals a linear relation between friction coefficients and rate of temperature rise,

$$\mu = 0.84 - 0.0069 \cdot T'. \tag{5}$$

The dependency of the frictional strength on the temperature rise most likely indicates an acceleration of transition from brittle regime to ductile regime associated with heating rate of the

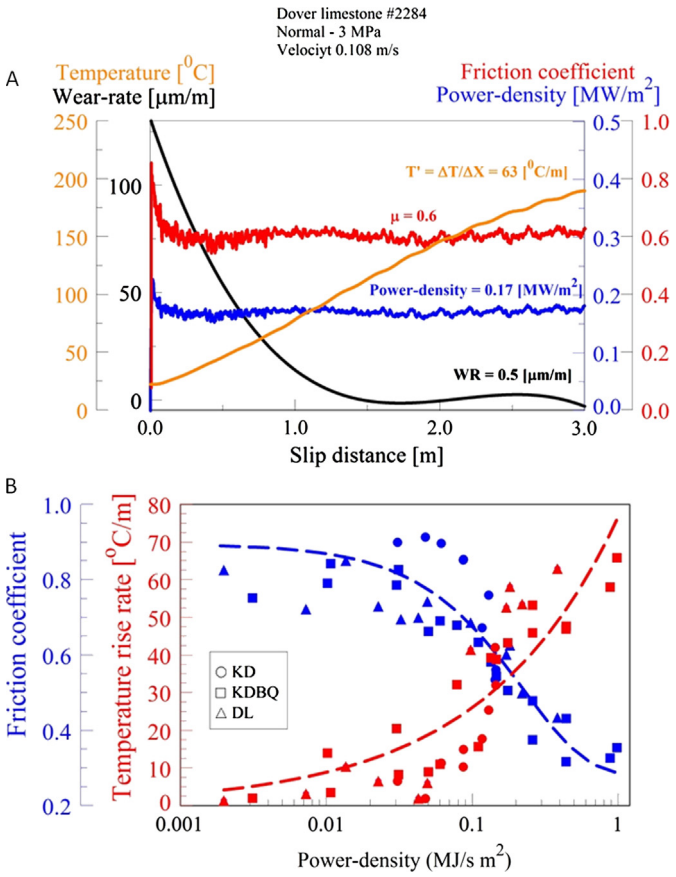

Fig. 10. A. Experimental evolution during steady-state experiment with Dover limestone; note that after ~1 m of slip, the power-density, friction coefficient, wear-rate and temperature slope all have quasi-constant values. B. Experimental relations between power-density PD and both friction coefficient, μ (blue), and temperature-rise-rate, T' (red). Results of 12 runs with dis-functioning thermocouples were excluded from this plot. Also plotted best fit curves (dashed lines of Eqs. (4) and (5) in the text). Note the inverse dependency of m and T' on PD.

fault surface. This transition is clearly recognized in the plot of friction coefficient as function of power-density (Fig. 5B), and in the friction-map plot (Fig. 8B). Fig. 5B shows high friction coefficients of $\mu > 0.8$ of the brittle regime of PD < 0.03, and friction coefficients of $\mu < 0.4$ of the ductile regime at PD > 0.3, and a brittle–ductile transition zone at PD $= 0.03$–0.3. The friction map (Fig. 8B) displays the friction coefficients as function of both σ_n and V; thus, PD cannot be directly plotted here. Instead, we plotted two lines of constant $\sigma_n \cdot V$, which is a proxy of power-density as PD $= \mu \cdot \sigma_n \cdot V$. In the friction map, the high friction of the brittle regime is bounded by $\sigma_n \cdot V < 0.1$, whereas the low friction of the ductile regime is bounded by $\sigma_n \cdot V > 0.3$. Further, the brittle–ductile transition is partly recognizable in the wear-map (Fig. 8A) in which intense wear-rates at low velocity and high normal stresses are associated with brittle deformation (blue background), mild wear-rates are associated with the ductile and transitional regimes (pink background).

Finally, it is important to note that the rheology which controls friction and wear is strongly depending on fault lithology. Our experiments were conducted on carbonate rocks (limestone, dolomite and dolomite–quartzite) under a moderate range of normal stresses ($\sigma_n < 7$ MPa) and wide range of velocities (up to 1 m/s). We found that both friction coefficient and steady-state wear-rates decrease at high velocities and high normal stresses (Figs. 4–7). Interestingly, Hirose et al. (2012) reached an opposite conclusion when measured the steady-state wear-rates of quartz-bearing faults (diorite, granite and sandstone) at normal stresses of 0.21 to 6.3 MPa, and slip velocity of 0.004 to 0.27 m/s. The cause for the apparent contradiction between the two studies is the different lithological composition of the faults. Reches and Lockner (2010) tested granite samples under a similar range as Hirose et al. (2012) and found that both friction coefficient and wear-rate drastically increased at slip velocities above ~0.05 m/s (Liao and Reches, 2012). Reches and Lockner (2010) demonstrated a direct link between frictional heating and the observed fault strengthening (their Fig. 3) that was interpreted as caused by dehydration of the brittle particles in the gouge (Sammis et al., 2011). We envision that at modestly elevated temperature (500–800 °C), quartz-bearing faults stay brittle and fail by thermal fracturing, whereas carbonate faults (and their gouge) at the same temperature range become more ductile and flow without fracturing. This apparent contradiction could be eliminated by having separate wear-rate map and friction map for different lithologies, as suggested above.

5. Conclusions

The present experiments were conducted on carbonate faults under a fairly wide range of slip velocities and normal stresses. We think that the conclusions below may also be applicable to other rock types, yet such application need to be demonstrated.

1. The steady-state wear-rates of faults depend on both normal loading and slip velocity, as presented on the wear-map (Fig. 8A), indicating a deviation from Archard's wear model. The wear-rates may practically vanish in a carbonate fault slipping at slip velocities comparable to earthquake slip-rates and at normal stresses of ~2–6 MPa.
2. The steady-state friction coefficients are best presented with respect to the mechanical power-density, PD $= \tau \cdot V = \sigma_n \cdot \mu \cdot V$ where τ, σ_n, μ and V are the shear stress, normal stress, friction coefficient, and slip velocity, respectively (Fig. 5).
3. Steady-state slip occurs at three-body mode under which a gouge layer separates the fault blocks, and the dominant fault wear is shifted to the gouge-rock contact.
4. In carbonate faults, the conversion of mechanical shear power into frictional heat causes a transition from brittle to ductile behavior of the gouge layer and the fault blocks.

Acknowledgements

Thanks to Andrew Madden, Shalev Siman-Tov and Xiaofeng Chen for the help and useful discussions. Harry Green kindly provided Fig. 7E. The thorough reviews and comments of Andrea Niemeijer and an anonymous reviewer significantly improved the manuscript. Support funds were provided by NSF Geosciences, Equipment and Facilities award 0732715, and NSF Geosciences, Geophysics award 1045414 to Z.R., and Israel Science Fund grant 929/10 to A.S.

Appendix A

A.1. Rotary shear apparatus (ROGA)

The present experiments were conducted on a rotary shear apparatus, referred to as ROGA. This experimental system is stationed in the School of Geology and Geophysics, Oklahoma University (Reches and Lockner, 2010). The system is designed to apply normal stresses up to 35 MPa, slip velocity in the range of 0.0003–2 m/s, and unlimited slip distance. The experimental fault behavior is recorded continuously including normal load, shear load, slip velocity, displacement normal to the fault surface, and sample temperature.

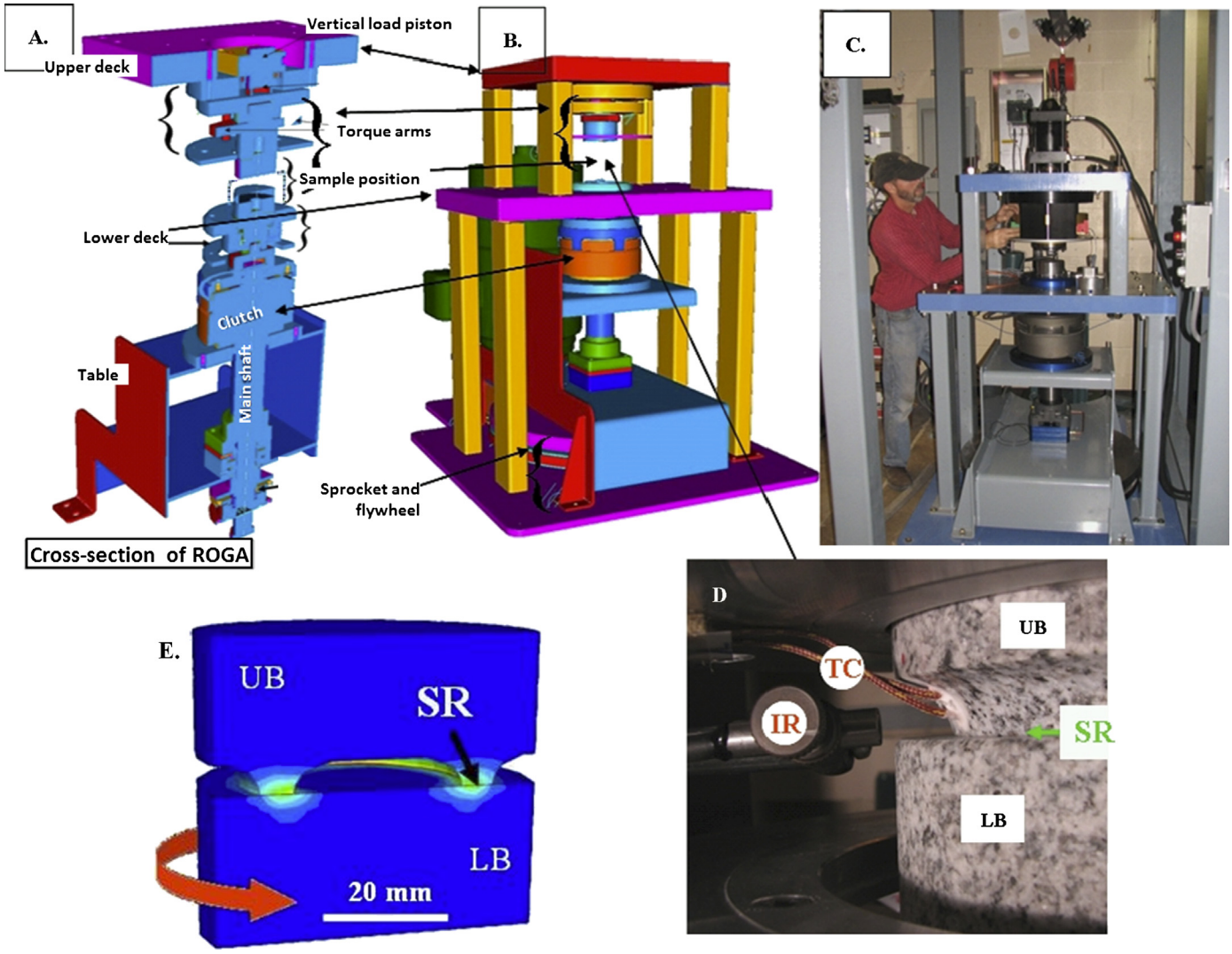

Fig. 11. The rotary shear apparatus. A. Cross section displaying power train. B. 3D view of the assembled apparatus. C. The apparatus with builder Joel Young. D. Sample blocks assembled in the loading frame. LB – lower block; UB – upper block; SR – sliding ring; TC – thermocouple wires; IR – infra-red sensor. E. Sample design shown as vertical cut-through of two cylindrical blocks of solid granite rock. The colors indicate temperature distribution due to frictional heating calculated using a finite-element model.

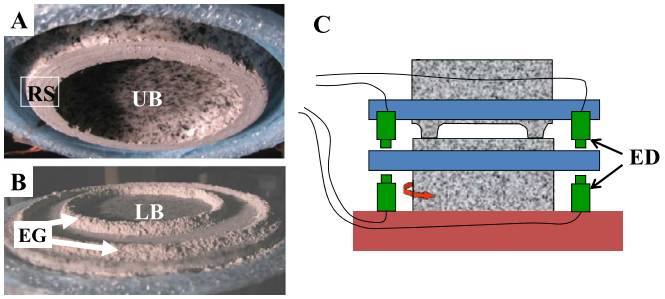

Fig. 12. A and B. Upper and lower block samples, marked UB and LB respectfully, after exposing the experimental (fault made of Sierra White granite). RS is the fault ring slip-surface on the upper block. EG is the ejected gouge which accumulated on the lower block at both sides of the ring slip-surface. C. A schematic cross section of the ROGA sample with the Eddy current (ED) sensors used for measuring the fault normal displacement (FND in text).

The apparatus frame is 1.8 m tall with two decks that are connected to each other by four internally enforced legs. The sample is placed between the two decks, and it is loaded by the rotary power train from below and by the normal stress from above. The power system includes:

(1) A 100 HP three-phase electric motor (Baldor-Reliance), and a Baldor VS1GV AC closed vector controller that provides constant torque of up to 2600 N m from 0 RPM to 3550 RPM. The shaft is powered by the motor with 1:6 velocity reduction sprockets.
(2) A 225 kg flywheel to boost the motor torque for short rise time during high-speed tests.
(3) An electro-magnetic large clutch (Ogura) that is capable of full engagement in 30 ms.
(4) A hydraulic piston system (Enerpac) with axial load up to 9500 N.

ROGA has National Instruments control and monitoring system with a SCXI-1100 with modules 1124 (analog control) 1161 (relay control), 1520 (load cell/strain gage), and 1600 (data acquisition and multiplexer), as well as a USB-6210 (encoder measurements). A dedicated LabView controls the system. Digital sampling rate is up to 10 kHz. Load-cells for axial load and torque (Honeywell), gouge dilation/compaction is measured with four eddy-current sensors (Lion Precision) (1-micron accuracy), temperature measurement is with thermo-couples (Omega), and sample radial velocity encoder of 8192 sectors (Sick-Stegmann).

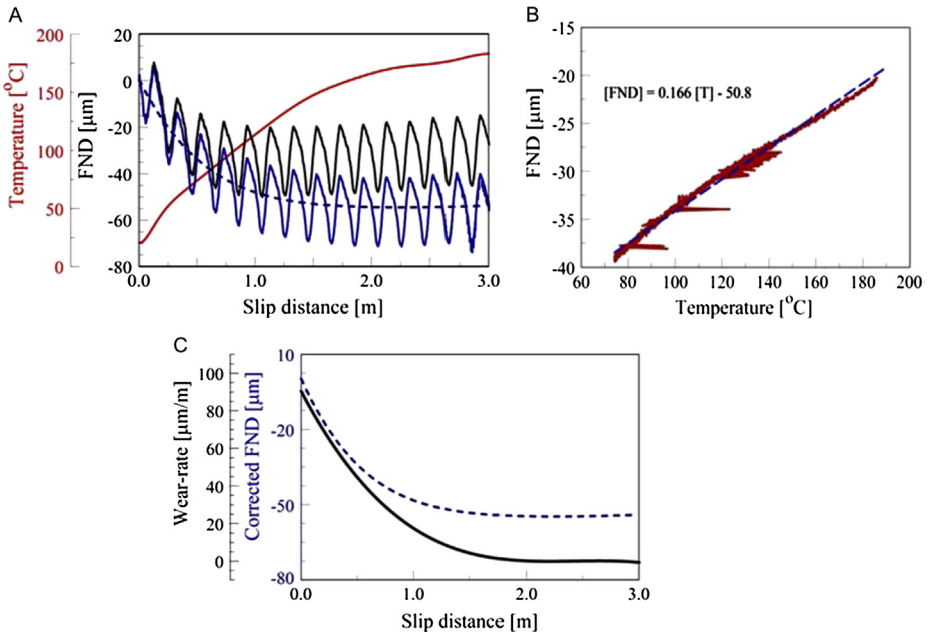

Fig. 13. Wear-rate calculations procedure for experimental results of Kasota dolomite sample sheared at $\sigma_n = 2.6$ MPa and $V = 0.05$ m/s. A. Raw FND data (cyclical black curve), and thermocouple measured temperature (red curve), corrected FND for thermal expansion (cyclical blue curve), and fitted polynomial curve (blue dashed line) to the corrected FND data. B. Measured FND as function of thermocouple temperature during post-slip, cooling stage; note reducing FND (closure) as the temperature drop. A linear fit (dashed blue line) indicates a slope of t = 0.166 μm/°C, and this constant was used to correct the raw FND data in A (see text). C. The fitted polynomial curve (blue dashed line) to the corrected FND data from A, and the calculated wear-rate (mm/m) (solid black curve) that is the derivative of the polynomial fit (see text). (For interpretation of the references to color in this figure, the reader is referred to the web version of this article.)

A.2. Wear-rate calculations

The wear calculations are based on the measurement of the Fault Normal Displacement (FND). The FND is the displacement normal to fault surface, measured by two sets of eddy-currents sensors (Fig. 12C). These are non-contact sensors, made by Lion's Precision that detect displacement due to change of the magnetic field with accuracy of ~1 μm. Each set of eddy-currents compose of two sensors facing each other (Fig. 12C), and located 180° to each other. The eddy-currents fixed to the upper block measure the height change with respect to the lower eddy-current fixed to the lower block. We define closure between the two blocks as negative FND and dilation as positive FND.

Some experiments show wobbling (Fig. 13A) caused by an imperfect alignment of the upper and lower axes of rotation. The wobbling wavelength is equal to sample circumference, which makes it easy to identify and to separate from real wear of the experimental fault.

Wear-rates throughout each experiment were calculated and corrected form the initial fault-normal-displacement (FND) in the following procedure:

The frictional heating during slip led to sample expansion and thus to an apparent dilation and position FND measurement. To correct for this thermal effect, we continued to measure both temperature and FND after slip cessation for 60–120 s. During this period, the sample cooled and contracted under the same normal load of the experiment. This contracting during cooling generated a quasi-linear relations between FND closure and thermocouple temperature decrease (Fig. 13B). We calculated the slope of the curve, t (units of μm/°C), and regarded t as an empirical thermal constant of sample dilation/contraction by heating/cooling. We used this constant to remove the thermal dilation component from the measured FND by calculating:

$$\mathrm{TW} = \text{Total wear } [\mu\mathrm{m}] = \mathrm{FND} + t \cdot \Delta T$$

where ΔT is the temporal increase of the thermocouple temperature. Fig. 13A displays the raw FND (black) and the thermally corrected FND (= total wear) in blue.

To minimize the effect of sample wobbling, the TW curve (blue in Fig. 13A) was fitted by a polynomial curve of order of 5–15 (dashed, blue curve in Figs. 13A and C). This fit removes the wobbling variations of TW.

The wear-rate is the local slope of the TW (total wear) with respect to the slip distance is calculated to derive the wear-rate with units of [μm/m]; the wear-rate indicates closure (negative) or dilation (positive) normal to the experimental fault per unit of slip distance (black curve in Fig. 13C).

To test the accuracy of this linearized procedure, we heated a granite sample with an electric heater (no slip or wear) while measuring the temperature and thermal induced FND as described above. The RMS of the difference between calculated and measured thermal FND is 3–10% of its total. Wear results are presented in geometric units: Wear is specified by microns of thermally corrected FND, and wear-rate is presented by μm/m, which is the wear per meter slip.

References

Archard, J.F., 1953. Contact rubbing of flat surfaces. J. Appl. Phys. 24, 981–988.
Barber, D.J., Wenk, H.R., Heard, H.C., 1994. The plastic deformation of polycrystalline dolomite: comparison of experimental results of theoretical predictions. Mater. Sci. Eng. A, Struct. Mater.: Prop. Microstruct. Process. 175, 83–104.
Biegel, R.L., Wang, W., Scholz, C.H., Boitnott, G.N., 1992. Micromechanics of rock friction. 1. Effects of surface roughness on initial friction and slip hardening in Westerly granite. J. Geophys. Res. 97, 8951–8964.
Boitnott, G.N., Biegel, R.L., Scholz, C.H., 1992. Micromechanics of rock friction. 2. Quantitative modeling of initial friction with contact theory. J. Geophys. Res. 97, 8965–8978.
Boneh, Y., Chang, J., Lockner, D.A., Reches, Z., submitted for publication. Fault evolution by transient processes of wear and friction. Pure Appl. Geophys.
Brown, K.M., Fialko, Y., 2012. 'Melt welt' mechanism of extreme weakening of gabbro at seismic slip rates. Nature 488, 638–641.
Byerlee, J.D., 1968. Brittle–ductile transition in rocks. J. Geophys. Res. 73 (14), 4741–4750.
Byerlee, J.D., 1978. Friction of rocks. Pure Appl. Geophys. 1163, 615–626.

Chang, J.C., Lockner, D.A., Reches, Z., 2012. Rapid acceleration leads to rapid weakening in earthquake-like laboratory experiments. Science 338, 101, http://dx.doi.org/10.1126/science.1221195.

Chen, X., Madden, A.S., Bickmore, B.R., Reches, Z., 2013. Dynamic weakening by nanoscale smoothing during high velocity fault slip. Geology 41, 739–742, http://dx.doi.org/10.1130/G34169.1.

Descartes, S., Berthier, Y., 2002. Rheology and flows of solids third bodies: background and application to an $MoS_{1.6}$ coating. Wear 252, 546–556.

Di Toro, G., Han, R., Hirose, T., De Paola, N., Nielsen, S., Mizoguchi, K., Ferri, F., Cocco, M., Shimamoto, T., 2011. Fault lubrication during earthquakes. Nature 471, 494–498.

Godet, M., 1984. The third-body approach: A mechanical view of wear. Wear 100, 437–452.

Green, H.W., Lockner, D.A., Bozhilov, K.N., Madden, A., Beeler, N.M., Reches, Z., submitted for publication. Nanometric gouge in high-speed shearing experiments: superplasticity? Trans. Am. Geophys. Union (Abstract #T31D-08).

Han, R., Shimamoto, T., Hirose, T., Ree, J., Ando, J., 2007. Ultralow friction of carbonate faults caused by thermal decomposition. Science 316, http://dx.doi.org/10.1126/science.1139763.

Han, R., Hirose, T., Shimamoto, T., 2010. Strong velocity weakening and powder lubrication of simulated carbonate faults at seismic slip rates. J. Geophys. Res. 115, B03412, http://dx.doi.org/10.1029/2008JB006136.

Handin, J., Hager, R.V., 1957. Experimental deformation of sedimentary rocks under confining pressure: Tests at room temperature on dry samples. Am. Assoc. Pet. Geol. Bull. 41, 1–50.

Handin, J., Heard, H.C., Magouirk, J.N., 1967. Effect of the intermediate principal stress on the failure of limestone, dolomite, and glass at different temperature and strain rates. J. Geophys. Res. 72, 611–640.

Heard, H.C., 1960. Transition from brittle fracture to ductile flow in Solenhofen limestone as a function of temperature, confining pressure, and interstitial fluid pressure. In: Griggs, D., Handin, J. (Eds.), Rock Deformation. In: Geol. Soc. Am. Memoirs, vol. 79, pp. 193–226.

Hirose, T., Mizoguchi, K., Shimamoto, T., 2012. Wear processes in rocks at slow to high slip rates. J. Struct. Geol., http://dx.doi.org/10.1016/j.jsg.2011.12.007.

Hutchings, I.M., 1992. Ductile–brittle transitions and wear maps for the erosion and abrasion of brittle materials. Appl. Phys. 25 (1A), A212, http://dx.doi.org/10.1088/0022-3727/25/1A/033.

Kishore Sampathkumaran, P., Seetharamu, S., Vynatheya, S., Murali, A., Kumar, R.K., 2000. SEM observations of the effect of velocity and load on the sliding wear characteristics of glass fabric-epoxy composites with different fillers. Wear 237, 20–27.

Kong, H., Ashby, M.F., 1992. Wear mechanisms in brittle solids. Acta Metall. 40, 2907–2920.

Liao, Z., Reches, Z., 2012. Modeling dynamic-weakening and dynamic-strengthening of granite in high-velocity. Chapter in "Earthquake Research and Analysis – New Advances in Seismology", Open access book.

Lim, S.C., 1998. Recent developments in wear-mechanism maps. Tribol. Int. 31, 87–97.

Lim, S.C., 2002. The relevance of wear-mechanism maps to mild-oxidational wear. Tribol. Int. 35, 717–723.

Lim, S.C., Ashby, M.F., Brunton, J.H., 1987. Wear-rate transitions and their relationship to wear mechanism. Acta Metall. 35, 1–24.

Ludema, K.C., 1996. Third bodies: Perspective on modeling in lubricated contacts, in close fitting contacts, etc., following on the concepts of Mr. Maurice Godet. Tribol. Ser. 31, 3–19.

Lyakhovsky, V., Sagy, A., Boneh, Y., Reches, Z., submitted for publication. Fault wear by damage evolution in a three-body slip mode. Pure Appl. Geophys.

Oohashi, K., Hirose, T., Shimamoto, T., 2011. Shear-induced graphitization of carbonaceous materials during seismic fault motion: Experiments and possible implications foe fault mechanics. J. Struct. Geol. 33, 1122–1134, http://dx.doi.org/10.1016/j.jsg.2011.01.007.

Power, W.L., Tullis, T.E., Weeks, J.D., 1988. Roughness and wear during brittle faulting. J. Geophys. Res. 93, 15268–15278.

Queener, C.A., Smith, T.C., Mitchell, W.L., 1965. Transient wear of machine parts. Wear 8, 391–400.

Rabinowicz, E., Dunn, L.A., Russell, P.G., 1961. A study of abrasive wear under three-body conditions. Wear 4, 345–355.

Reches, Z., Lockner, D.A., 2010. Fault weakening and earthquake instability by powder lubrication. Nature 467, 452–456.

Resor, P.G., Meer, V.E., 2009. Slip heterogeneity on a corrugated fault. Earth Planet. Sci. Lett. 288, 483–491.

Sagy, A., Brodsky, E.E., 2009. Geometric and rheological asperities in an exposed fault zone. J. Geophys. Res. 114, B02301, http://dx.doi.org/10.1029/2008JB005701.

Sammis, C.G., Ben-Zion, Y., 2008. Mechanics of grain-size reduction in fault zones. J. Geophys. Res. 113, http://dx.doi.org/10.1029/2006JB004892.

Sammis, C., Lockner, D., Reches, Z., 2011. The role of adsorbed water on the friction of a layer of submicron particles. Pure Appl. Geophys. 168, 2325–2334.

Scholz, C.H., 1987. Wear and gouge formation in brittle faulting. Geology 15, 493–495.

Siman-Tov, S., Aharonov, E., Sagy, A., Emmanuel, S., 2013. Nano-grains form carbonate "fault mirrors". Geology, http://dx.doi.org/10.1130/G34087.1.

Smith, S.A.F., Di Toro, G., Kim, S., Ree, J.-H., Nielsen, S., Billi, A., Spiess, R., 2013. Coseismic recrystallization during shallow earthquake slip. Geology 41 (1), http://dx.doi.org/10.1130/G33588.1.

Soda, N., Kimura, Y., Tanaka, A., 1975. Wear of some F.C.C. metals during unlubricated sliding. Part I. Effects of load, velocity and atmospheric pressure on wear. Wear 33, 1–16.

Stupak, P.R., Kang, J.H., Donovan, J.A., 1990. Fractal characteristics of rubber wear surfaces as a function of load and velocity. Wear 141, 73–84.

Vingsbo, O., Soderberg, S., 1988. On fretting maps. Wear 126, 131–147.

Wang, D.Z., Peng, H.X., Liu, J., Yao, C.K., 1995. Wear behavior and microstructural changes of SiCW–Al composite under lubricated sliding friction. Wear 184, 187–192.

Wang, W.B., Scholz, C.H., 1994. Wear processes during frictional sliding of rock – a theoretical and experimental study. J. Geophys. Res. 99, 6789–6799.

Wilson, B.T., Dewers, T., Reches, T., Brune, J.N., 2005. Particle size and energetics of gouge from earthquake rupture zones. Nature 434, 749–752.

Yoshioka, N., 1986. Fracture energy and the variation of gouge and surface roughness during frictional sliding of rocks. J. Phys. Earth 34, 335–355.